catalysts

MDPI

Article

A 'Defective' Conjugated Porous Poly-Azo as Dual Photocatalyst

Ipsita Nath [1,2,*], Jeet Chakraborty [1,2,*], Sara Abednatanzi [1] and Pascal Van Der Voort [1,*]

[1] Department of Chemistry, Center for Ordered Materials, Organometallics and Catalysis (COMOC), Ghent University, 9000 Ghent, Belgium; sara.abednatanzi@ugent.be
[2] Eco-Friendly Applied Materials Laboratory (EFAML), Materials Science Centre, Department of Chemical Sciences, Indian Institute of Science Education and Research-Kolkata, West Bengal 741246, India
* Correspondence: ipsita.nath@hotmail.com (I.N.); jeet.chakraborty@hotmail.com (J.C.); pascal.vandervoort@ugent.be (P.V.D.V.)

Abstract: A heterogeneous photocatalyst amenable to catalyze different chemical reactions is a highly enabling and sustainable material for organic synthesis. Herein we report the synthesis and characterization of an azobenzene-based organic π–conjugated porous polymer (AzoCPP) as heterogeneous dual photocatalyst manifesting net-oxidative bromination of arenes and dehydroxylation of boronic acids to corresponding phenols. Hierarchical porosity and high surface area of the nano-sized AzoCPP allowed superior catalyst-substrate contact during catalyses, whereas the inherent structural defect present in the CPP backbone resulted in low-energy sinks functioning as *de facto* catalytic sites. A combination of these two structure-property aspects of AzoCPP, in addition to the dielectric constant manipulation of the system, led to excellent catalytic performance. The protocols remained valid for a wide substrate scope and the catalyst was recycled multiple times without substantial loss in catalytic activity. With the aid of subsequent control experiments and analytical characterizations, mechanisms for each catalysis are proposed and duly corroborated.

Keywords: conjugated porous polymer; azobenzene; photocatalysis; nanoparticle; structural defect; exciton diffusion; mechanism

check for updates

Citation: Nath, I.; Chakraborty, J.; Abednatanzi, S.; Van Der Voort, P. A 'Defective' Conjugated Porous Poly-Azo as Dual Photocatalyst. *Catalysts* **2021**, *11*, 1064. https://doi.org/10.3390/catal11091064

Academic Editor: José María Fraile

Received: 11 August 2021
Accepted: 30 August 2021
Published: 31 August 2021

Publisher's Note: MDPI stays neutral with regard to jurisdictional claims in published maps and institutional affiliations.

Copyright: © 2021 by the authors. Licensee MDPI, Basel, Switzerland. This article is an open access article distributed under the terms and conditions of the Creative Commons Attribution (CC BY) license (https://creativecommons.org/licenses/by/4.0/).

1. Introduction

Conjugated porous polymers (CPPs) are metal-free, exceptionally stable, permanently nanoporous, amorphous materials with high surface area, which are constructed by chemical tying of organic monomer(s) acting as linkers and knots [1–9]. The kinetically controlled irreversible synthesis of CPPs endow high structural disorder, inhomogeneity, and defects, e.g., non-uniform bond order, skeletal twisting, chain-pore interpenetration, incomplete polymer chain propagation, unintended chain branching, etc. leading to an innately amorphous coarse structure. Therefore, despite being infinitely π–conjugated, the true 'conjugation' operates only within small sections of the entire skeleton that roughly abide by the 'Hückel's rule' [10]. In fact, the whole conjugated backbone has been proven to show only a little influence on the catalytic performance of a CPP than the local conjugated environment around the active catalytic unit [11].

On the positive note, however, CPPs provide us with a wide molecular catalog to choose the constituent monomers from, which functions as the *de facto* active catalytic units of the daughter polymers. This allows manual tuning of the photophysical and electrochemical property of the materials for targeted application/catalysis (much like a molecular catalyst) [4,5]. These two structural aspects of CPPs make them a unique class of heterogenized molecular photocatalyst with added semiconducting elements [10]. This property of CPPs has been widely exploited for an array of organic reactions going through photoredox and/or energy transfer pathways, e.g., oxidative and reductive coupling, singlet

oxygen-mediated reactions, etc. as well as for energy applications, e.g., water splitting and CO_2 reduction, and wastewater treatment [2–5]. Among various building units, azobenzenes have recently acquired significant attention for photo-responsive polymer and CPP synthesis. The photo-triggered *cis-trans* isomerization of azobenzenes have been widely exploited in flexible polymer-based photonic crystals [12,13]. On the other hand, the near-UV active azobenzenes are also routinely incorporated into skeletally rigid conjugated CPP backbones to manifest conjugation-induced enhanced visible-light-response. It has been recently shown that azobenzene containing CPPs are excellent candidate for transition metal chelation, photocatalytic C-C coupling, and selective hydrogenation [14–16]. However, in most of these cases, the CPP is custom-designed to promote only a single catalytic assay. Irrespective of great practical, industrial, and economic value, CPPs stimulating more than one catalysis have rarely been reported [17–19].

As in semiconductors, photo-illumination triggers exciton pair generation in the CPP skeletons, which must travel to the nearest catalytic center as mobile charge-carriers to participate in the catalysis [20]. Therefore, high surface area and porosity play decisive roles in augmenting catalyst-substrate contact to facilitate catalyst-to-substrate charge/energy transfer [21]. However, porosity also decreases the dielectric constant (ε_r) of the material, which is inversely proportional to the exciton binding energy [22]. For organic CPPs, ε_r values are intrinsically small resulting in strongly bound exciton pairs, where added porosity may pose a supplementary detrimental effect in charge-carrier separation and mobility [23]. As a result of these two opposing factors and discontinued skeletal conjugation, unlike the through-band charge-carrier transport of traditional semiconductors, a 'partial through-band, partial hopping'-type hybrid mobility of charge (i.e., electron and hole) occurs in CPPs over a small exciton diffusion distance [24]. The structural defects play a beneficial role in exciton separation by trapping free polarons, or the distinct charge-carrier itself [25–27]. These traps can be classified as deep-traps and swallow-traps depending on the extent of defects (related to chain connectivity and secondary chemical backbone modification) that result in further localized energy levels in the electronic bandgap of the material enabling low energy photon absorption and emission. Evidently, these defect-sites can be regarded as independent catalytic energy-sinks, if housed within the reach of the mobile substrate in the medium [27]. However, this also infers a greater chance of exciton recombination, and a rapid charge or energy transfer to the substrates/reactants is an obligation to achieve high quantum efficiency [28].

In light of this, it is envisaged that fabricating high surface area CPPs as small-sized particles and exploiting their inherent structural defects can augment charge separation and mobility while rendering increased catalyst-substrate contact [29,30]. A high surface area also infers dense defect population, an instrumental quality for maximized photo-energy exploitation. Additionally, using a suitably chosen solvent (one having high ε_r) that can percolate through the CPP pores will increase the effective ε_r of the system, enhancing the relative exciton diffusion distance [10]. In this work, we comprehensively exploit these effects through synthesizing azobenzene-based CPP (AzoCPP) nanoparticles as a defect-dense hierarchically porous photocatalyst for (i) oxidative aromatic bromination and (ii) boronic acid dehydroxylation. The structure–property relationship of the material with its photo-response is thoroughly tied and discussed. The highly defective backbone of the polymer resulted in intrinsic energy traps/sinks and rapid exo-skeletal charge transfer from polymer to reactants/sacrificial agents enhancing the catalytic propensity of the material.

2. Results and Discussion

2.1. Synthesis and Characterizations

AzoCPP was synthesized by $Pd(PPh_3)_2Cl_2$ catalyzed Cu-free Sonogashira coupling of highly diluted *E*-4,4'-diiodoazobenzene and 1,3,5-triethynyl benzene under rapid stirring (Scheme 1). The Cu-free protocol was purposely adopted to mitigate Glaser homocoupling of the ethynyl ends, furnishing constrained Pd-catalysis-mediated polymer chain termination and defect generation. It also helped with slow alkyne activation during

CPP synthesis (i.e., constrained Pd-catalysis), which was further enhanced by the nominal catalyst-substrate contact imposed by highly-diluted reaction conditions. This critical synthetic-condition-engineering along with rapid stirring of the medium decreased the polymer formation and propagation rate and produced AzoCPP as an ensemble of tiny amorphous particles.

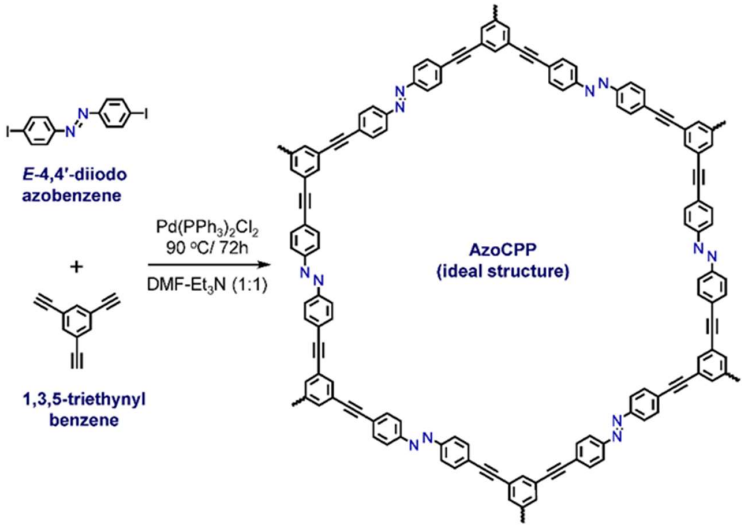

Scheme 1. Synthetic route to AzoCPP.

The field emission scanning electron microscope (FESEM) image of AzoCPP showed ca. 50–100 nm-sized polymer particles (Figure 1a), which was further corroborated by the transmission electron microscope (TEM) image (Figure 1b). The tiny particulate appearance of the material was better articulated from the 3D topographic mapping of the selected area from the TEM image (Figure 1c,d). On the other hand, the amorphous nature of AzoCPP was confirmed from its characteristic broad x-ray diffraction (XRD) pattern originating from long-range structural disorder (Figure S1).

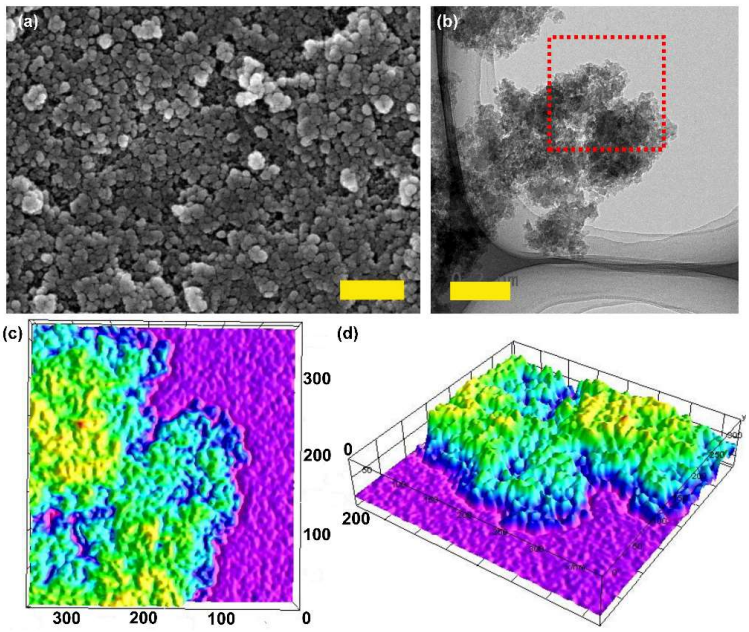

Figure 1. (**a**) FESEM image of AzoCPP, scale bar 500 nm; (**b**) TEM image of AzoCPP, scale bar 200 nm; (**c**) top view and (**d**) side view of 3D topological mapping of the selected area of AzoCPP TEM image (red box) with the scale calibrated to actual particle size (in nm).

Solid-state ^{13}C NMR (SS-NMR) provided structural corroboration of the polymer network. The characteristic peaks for the alkyne and N-bound carbons appeared at 93.1 and 153.8 ppm respectively. On the other hand, the highly superimposed signals from other aromatic carbons were deconvoluted into four distinct peaks. Figure 2a (inset) shows the chemical structure of the repeating unit of AzoCPP with different carbons color-coded into corresponding NMR signals. Another notable observation from the SS-NMR spectrum was the existence of additional unaccounted low-intensity peaks (shaded section in Figure 2a) apart from the spinning sidebands (denoted by '★') [31]. These peaks were classified into two categories, the ones shaded in red were ascribed to a small fraction of the unreacted terminal alkynes (due to the constrained reaction condition), whereas the yellow-shaded bands were possibly originated from other untraceable structural defects, inherent to CPPs.

The Fourier transformed infrared (FTIR) spectrum of the material further supported these structural annotations. Typical bands originating from the asymmetric stretching of aromatic C=C and C–H, and C≡C appeared at 1575, 2923, and 2185 cm^{-1} respectively (Figure 2b), whereas the band at 845 cm^{-1} was ascribed to the C–N bending mode. An interesting observation, however, was the appearance of asymmetric C=N stretching peak at 1668 cm^{-1} inferring an extensive local conjugation at the azo-sites. A very low-intensity peak was also observed at 3058 cm^{-1} corresponding to the asymmetric stretch of the terminal alkyne C–H, justifying the SS-NMR observations.

The non-local density functional theory (NLDFT) calculated from Ar sorption isotherm of AzoCPP showed that the anisotropic 3D connectivities and built-in structural defects in the material resulted in highly hierarchical pores (Figure 2c). A total 801 m^2/g Brunauer–Emmett–Teller (BET) surface area was calculated from the low relative pressure region of the Ar-sorption isotherm of the polymer (Figure 2c, inset) with a total pore volume of 0.59 cm^3/g. A mesopore/micropore ratio of 3:1 was obtained indicating an extensive abundance of mesopores over micropores, congruent to the NLDFT plot. This observation can be explained considering the synthetic strategy-mediated chain termination and defect formation that led to larger pore dimensions. The wide hysteresis present in the sorption isotherm offered auxiliary support to the high mesopore content by endorsing strong multilayer adsorption, a typical phenomenon for mesoporous materials.

The large molecular backbone, disordered structure and anisotropic chain propagation makes pinning of the intrinsic defect-sites with complete certainty difficult for CPPs. The current state-of-the-art analytical facilities are suitable to study defects only in high-purity molecular crystals, but lack the precision to specify the defects in innately amorphous materials. However, an intuitive picture can be drawn from other auxiliary assessments, e.g., XPS, porosity measurement, SS-NMR, FTIR, etc. The existence of unreacted terminal alkynes in AzoCPP has already been confirmed from FTIR and SS-NMR. This, and the presence of extensive inherent mesopores collectively suggest improper polymer chain propagation and termination. A schematic illustration given in Figure 2e shows the ideal pore of AzoCPP (I), and various large pores and long chains of the material (II-IV) all maintaining the ⋯ABAB⋯ type cross-coupled connectivities. One can envision that the geometric constrains of these long chains and large pores will compel chain termination at certain points, whereas the flexibility of these large pores and chains in addition to the bond torsion may also allow alternate chain branching in 3D (red dots, Figure 2e). Notably, the situations depicted in Figure 2e are a speculative and simplistic take on the actual scenario, where extremely intricate and complex topology is obtained in practice due to previously mentioned inherent defects in CPP.

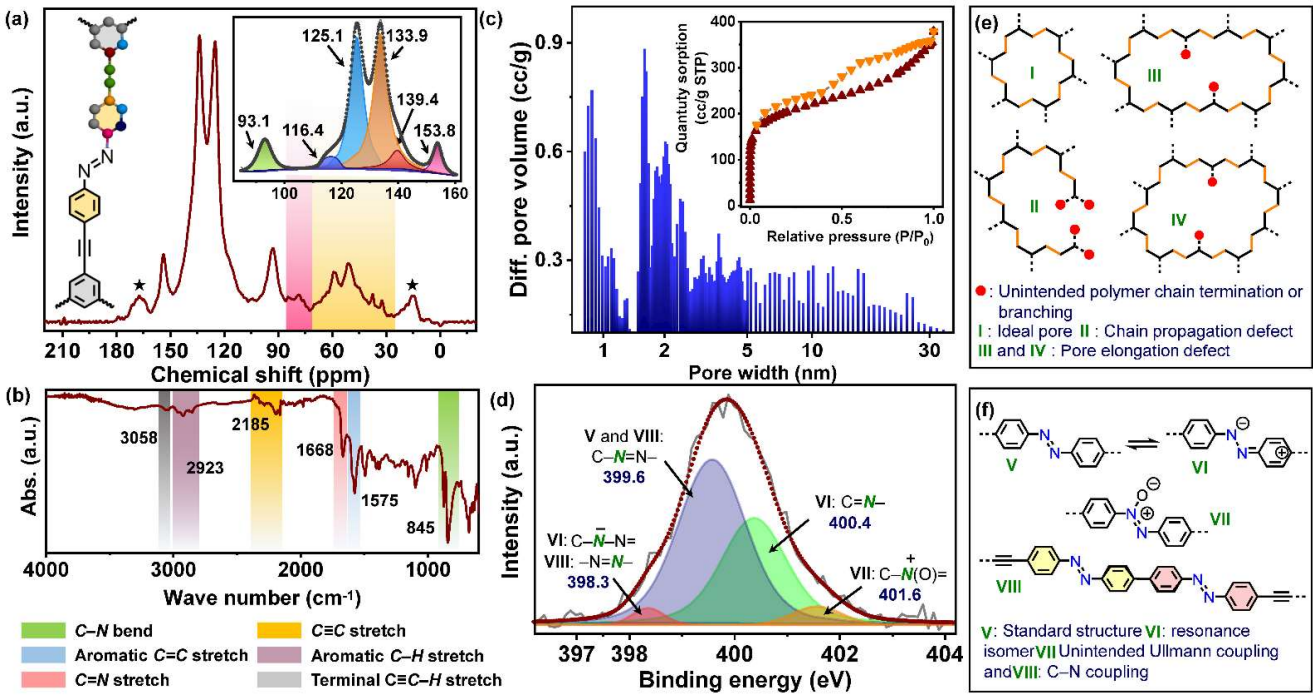

Figure 2. (**a**) Solid-state ^{13}C NMR spectrum of AzoCPP with the chemical backbone of the polymer repeating unit and corresponding color-coded NMR deconvolution peaks (inset); (**b**) FTIR spectrum of AzoCPP highlighting major IR bands; (**c**) the hierarchical porosity distribution of AzoCPP as obtained from NLDFT calculation and corresponding Ar sorption isotherm (inset); (**d**) deconvoluted N1s XPS spectra; and the intuitive polymer defects originating from (**e**) inefficient chain propagation and (**f**) unintended chemical reactions.

On the other hand, some defects may also arise from unintended chemical reactions in the polymer scaffold. The N1s XPS spectrum of AzoCPP can be deconvoluted into four bands arising from both targeted backbone and the chemical defects (Figure 2d). The standard azobenzene unit V (Figure 2f) can undergo resonance isomerization to VI. FTIR spectra of AzoCPP has already proven the existence of C=N functionality, essentially arising from VI. Accordingly, N1s XPS showed C–N (V) and C=N (VI) bands at 399.6 and 400.4 eV, respectively. The azobenzenes are also known to form N-oxide (VII, Figure 2f) upon exposure to air and moisture. Consequently, a high energy band was found at 401.6 eV in N1s-XPS, which was attributed to the cationic N-species of the N-oxide. Additionally, O1s XPS of the material has been deconvoluted as well to substantiate this claim (Figure S2). The CPP synthetic condition may favor Ullmann homocoupling of the azobenzene as well to some extent through Pd-catalyzed C-I bond cleavage (VIII, Figure 2f). Such homocoupling leads to a highly twisted biphenyl unit impeding extended conjugation. This would, in turn, result in relatively electron-rich azo-functionality (VIII) than the standard one (i.e., V), demonstrating a low energy N1s XPS peak (398.3 eV).

2.2. Photophysical and Electrochemical Properties

The photophysical and electrochemical analysis of AzoCPP was then conducted to deduce the structure-property relations, specifically the electronic effects imposed by the physicochemical defects. Comparative UV-Vis spectra of the azo-monomer and AzoCPP manifested a significant 53 nm redshift of the π–π^* absorption maxima (from 347 nm to 400 nm) and an overall increase in total photo-absorption cross-section upon polymerization (Figure 3a). This was a clear indication of the extended π–conjugation in the system compared to the pristine monomer, which made the exciton pair mobile upon photo-illumination over a larger molecular plain and decreased the overall energy gap [32]. Corresponding Tauc plot (Figure 3a, inset) confirmed an optical bandgap of 2.56 eV. The electronic energy gap, on the other hand, was obtained from cyclic voltammogram (CV) experiments, where the band-edge potentials

were calculated from the redox onsets of AzoCPP (*vs* SCE). Accordingly, 1.99 V oxidation and −0.50 V reduction potentials (i.e., valance and conduction band, VB-CB) were recorded for the material (Figure S3). The highest occupied and lowest unoccupied molecular orbital (HOMO-LUMO) deduced for the extended organic network showed that the HOMO was distributed throughout the planner conjugated skeleton, whereas the LUMO was centered on the azobenzene moiety (Figures S4 and S5). This accorded well with the UV-Vis spectrum of AzoCPP theoretically justifying the redshift.

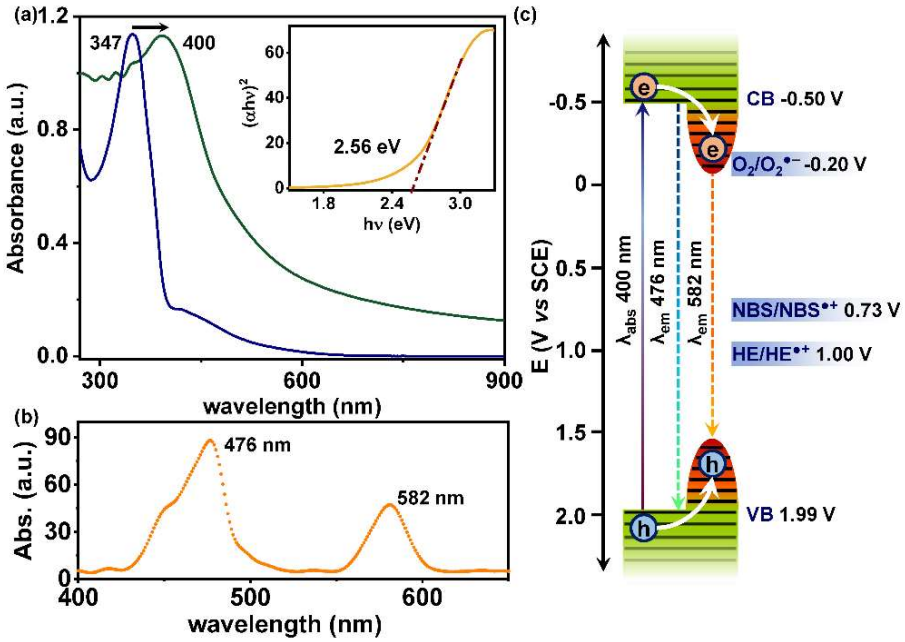

Figure 3. (**a**) The UV-Vis absorption spectra of the azo-monomer (blue) and AzoCPP (green) demonstrating the redshift in absorption maxima and corresponding Tauc plot (inset); (**b**) fluorescence spectrum of the polymer showing standard and defect-induced emission; and (**c**) schematic depiction of the entire photon absorption and emission scenario with VB-CB shown in green and defects shown in red shading.

The emissive property of the polymer analyzed by fluorescence spectroscopy provided interesting insights. As depicted in Figure 3b, the material demonstrated two distinct emission bands, one centering at 476 nm and another significantly low-energy band at 582 nm. The former peak at 476 nm was ascribed to the true emission from the *trans*-azo-unit of the CPP, whereas the appearance of the low-energy one can be explained considering the reduced bandgap at the defect sites due to the generation of energy sinks [33–35]. Though the *cis*-isomer of azobenzene also emits at a higher wavelength, the constrained degree-of-freedom of AzoCPP resulting from strongly coupled azobenzene as struts in the rigid organic backbone will not allow the isomeric photo-transition to occur in the polymer scaffold [32]. This defect-induced emission theory was consistent with the aforementioned analytical assessments and literature [29,30,33–35]. The situation is schematically depicted in Figure 3c, where both VB and CB were shown to be associated with defect sites (red) as an extreme tentative scenario.

The electron paramagnetic resonance (EPR) spectra of AzoCPP were recorded both in dark and visible light (Figure S6). The increase in the intensity of the Lorentzian lines after photo-illumination proved the photo-responsive nature of the polymer. However, the extent of this intensity increment was about 23% compared to ca. 50% or even more for other semiconducting systems inferring rapid recombination of the charge-carriers [36]. This observation is congruent to the structural defect argument and emission spectrum of the polymer. A *g*-factor of 2.0043 was calculated, which is slightly higher than the free electron (2.0023) suggesting that the exciton pairs in AzoCPP indeed overcame the exciton

binding energy upon photo-irradiation to became free charge-carrier with augmented motility (possibly due to local conjugation), and can be exploited for photocatalytic activity.

2.3. Photocatalysis

2.3.1. Oxidative Bromination

Aryl bromides are important synthons for a variety of value-added organic compounds, drugs, and natural products whose synthesis mostly requires toxic and carcinogenic Br_2 [37]. Though some bromination reactions can be achieved using N-bromo succinimide (NBS) as the Br-source, the scope for such reactions are rather limited and mandates long reaction time and harsh condition. With the experimental characterizations and analytical insights, AzoCPP was employed as a redox-catalyst for visible-light-mediated rapid aromatic bromination of a wide variety of electron-rich arenes with NBS at room temperature (Figure 4a).

Using naphthalene as the screening substrate, various solvents, and substrate concentrations were optimized to obtain the standard reaction condition, i.e., 0.1 mmol substrate, 0.2 mmol NBS, 5 mg AzoCPP, 1.5 mL acetonitrile/water (2:1), air atmosphere, and light (λ = 400 nm) to synthesize 1-bromonaphthalene as the sole product in 5 h (Table S1). The 400 nm light was chosen to directly induce the π–π^* transition in the material. Of note, the traditional bromination of naphthalene requires Br_2 as the Br-source and is difficult to control at the mono-bromination stage [38].

To deduce the reaction mechanism, a set of additional analytical and control experiments were performed (Table S2). To confirm the role of AzoCPP, a control experiment was conducted without employing the catalytic material, which yielded no detectable product within 5h. Notably, freshly procured NBS (white) was used for this purpose to avoid any contribution from the Br_2 impurity that gradually develops in NBS via self-decomposition over time. Similarly, switching off the light or running the reaction in the N_2 atmosphere resulted in only nominal amounts of products. The residual electronic activity of the material in dark (see EPR, Figure S6) or the traces of O_2 remained in the reaction container even after N_2 purging could be the contributing factor for these nominal reactivities. Additionally, the redox potentials of AzoCPP were sufficient to oxidize NBS to corresponding radical cation (E_{ox} 0.73 V vs. SCE) and reduce O_2 from air to $O_2^{\bullet-}$ (Figure 3c).

With these experimental proves and assessments, an oxidative photo-redox mechanism is proposed (Figure 4b). Upon photo-illumination, the excited AzoCPP* oxidized NBS to corresponding N-radical cation species (**A**) that enhanced the electrophilic property of the adjacent Br [39]. A subsequent nucleophilic substitution with arenes functioning as nucleophiles generated the cationic intermediate **B**. The reduced AzoCPP, on the other hand, converted to its parent form by reducing aerial O_2 to $O_2^{\bullet-}$, which deprotonated **B** to produce the final brominated product. Succinimide and H_2O_2 were generated as the by-products. The appearance of succinimide was confirmed from GC, whereas the occurrence of H_2O_2 was chemically proven. As shown in Figure 4c, in a solution of glacial acetic acid in aqueous KI, two drops of the reaction mixture were added resulting in rapid brown coloration. After adding more drops and a gentle shake, the whole mixture turned brown. On the other hand, when commercial H_2O_2 was added to the initial solution as a control, it also had the same coloration. This is a qualitative proof of the standard acid-catalyzed reaction of iodide and H_2O_2 to generate brown I_2 that justified the occurrence of H_2O_2 in the said mechanistic protocol. Additionally, the EPR spin trapping experiments were also conducted in acetonitrile with 5,5-dimethyl-1-pyrroline N-oxide (DMPO) as the $O_2^{\bullet-}$ trapping agent to experimentally confirm the mechanism. Figure S7 shows that pure AzoCPP in acetonitrile produced a strong EPR signal for DMPO-superoxide adduct corroborating the polymer's ability to mono-reduce O_2. The spectral pattern remained almost unaltered after the addition of naphthalene followed by 15 min photo-illumination. However, further addition of NBS and 15 more min of photo-irradiation drastically decreased the peak intensity inferring the involvement of $O_2^{\bullet-}$ in the reaction protocol.

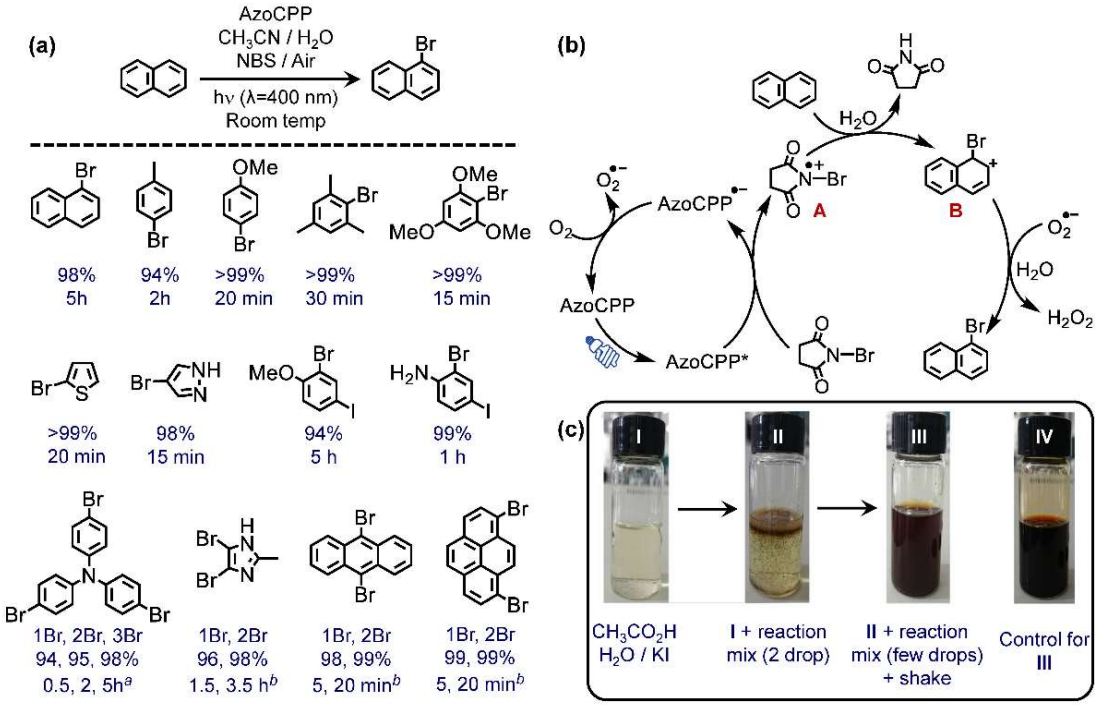

Figure 4. (**a**) Photocatalytic bromination of arenes with corresponding substrate scope and product yields (GC), [a] 3 times more NBS was used, [b] 2 times more NBS was used; (**b**) proposed mechanism for the reaction; and (**c**) qualitative proof for H_2O_2 generation.

The substrate scope of the catalytic protocol was then studied. As depicted in Figure 4a, the method worked perfectly for electron-rich arenes. The proposed mechanistic pathway also supports this, as an electron-donating arene would function better as a nucleophile. Owing to this justification, toluene showed faster catalytic activity than naphthalene, whereas anisole outperformed them both. Of note, only *para*-substituted products were obtained in each case. The steric hindrance that the *ortho*-substituted products had to endure at the intermediate stage (i.e., during **A**→**B** formation) possibly triggered such quantitative regioselectivity. However, a tread-off between the steric effect and electron-donating effect was observed for more bulky, yet electron-rich 1,3,5-xylene and 1,3,5-trimethoxy benzene. In each of these two cases, despite strong steric hindrance, a rapid bromination was observed indicating a more decisive role of the electron-donating functionality than their steric bulk. A similar activity was maintained for heteroarenes as well. Subjecting *para*-iodoaniline and *para*-iodoanisole also resulted in the corresponding brominated product. These are of great interest because the presence of both bromo and iodo functionality would allow a selective follow-up coupling. Playing with the NBS concentration allowed multiple brominations in triphenylamine, 2-methyl imidazole, pyrene, and anthracene. As demonstrated in Figure 4a, very selective step-wise bromination was observed in all cases with yield for mono-bromination reaching more than 94% before the second bromination started. This was a crucial observation as it would provide a time-dependent control on the product selectivity. Of note, bromination of some of these substrates (e.g., anthracene, anisole, etc.) can indeed be done with NBS alone without any catalyst or light. However, those processes are rather slow, less bench-top productive, and selective. On the other hand, this method not only makes the process better performing but significantly enhances the range of substrates that can be benefited from the protocol.

2.3.2. Oxidative Dehydroxylation of Boronic Acids

To establish the dual catalytic nature of AzoCPP, it was further subjected to catalyze oxidative dehydroxylation of boronic acids to form corresponding aryl alcohols (Figure 5a). Using phenylboronic acid as the substrate, various solvents, and amines (and equivalence)

were thoroughly screened to obtain the optimized condition, i.e., 0.1 mmol substrate, 0.15 mmol Hantzsch ester (HE), 2 mL acetonitrile/water (4:1), 5 mg AzoCPP, 1 atm O_2, 1d, and light (λ = 400 nm) (Table S3). The mechanism, consistent with the literature [18,19], showed the role of HE as a hole scavenger and hydrogen atom transfer (HAT) catalyst. Upon photo-illumination, excited AzoCPP* oxidized HE (E_{ox} 1.0 V vs. SCE) to corresponding radical cation. The reduced catalyst then returned to its original state by reducing O_2 to $O_2^{\bullet-}$. The superoxide so formed attached to the electron-deficient p-orbital of B present in the boronic acid to generate intermediate **C** (Figure 5b). The HE radical cation then functioned as a HAT catalyst to convert **C** to **D**. Finally, **D** underwent a Petasis-type reaction giving alcohol as the final product. Similar to the previous bromination reaction, EPR spin trapping experiments were conducted to confirm the mechanism for dehydroxylation as well. Figure S7 depicts that the addition of phenylboronic acid in an acetonitrile dispersion of AzoCPP led to a significant decrease in the DMPO-superoxide adduct signal. This observation is a clear indication of the boronic acid-$O_2^{\bullet-}$ adduct formation in situ during the catalytic assay. This observation, which accords well with the literature reports [18,19], provided experimental backing to the proposed reaction mechanism. Control experiments performed without employing the catalyst or HE failed to produce any product, whereas only a trace product was obtained in dark, further endorsing the critical role of each of these catalytic partners (Table S4).

The substrate scope for the catalysis was then tested (Figure 5a). Phenylboronic acids containing both electron-donating and withdrawing *para*-substitutions manifested equipotent activity confirming no obvious role of electronic effect in the protocol. The steric effect imposed by *ortho*-substitution also had only a nominal impact as both 2-bromo and 2-isopropyl phenylboronic acids were facilely converted to corresponding phenols. The reactivity, however, dropped considerably for polyboronic acids. For example, 1,4-phenyldiboronic acid gave 78% yield of the desired 1,4-benzoquinol after 2d, whereas phenyl-1,3,5-triboronic acid converted to cyclohexane-1,3,5-trione with 66% yield in 3d.

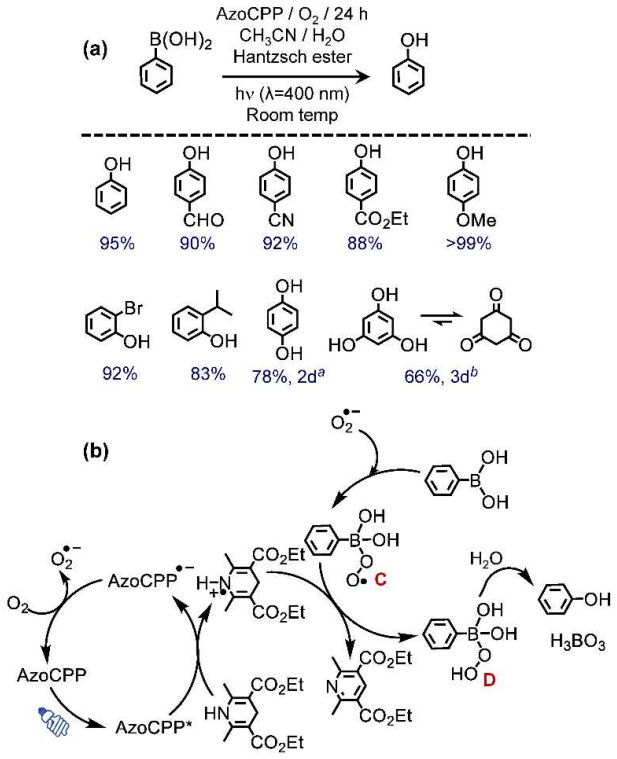

Figure 5. (**a**) Photocatalytic dehydroxylation of aryl boronic acids to alcohols with corresponding substrate scope and product yields (GC), [a] 2 times more HE was used, [b] 3 times more HE was used; (**b**) proposed mechanism for the reaction.

2.3.3. Structure–Property–Catalysis Interplay at AzoCPP

With these catalytic results and structure-property characterizations of AzoCPP, a clear interplay between these three can be portrayed. Illuminating AzoCPP with a 400 nm lamp indeed trigged a π–π* photo-absorption and consequent exciton pair generation as confirmed from the UV-Vis, fluorescence, and EPR spectroscopy. The theoretically calculated HOMO and LUMO orbital diagrams also demonstrated the existing electronic conjugation throughout the planer π–conjugated backbone of the CPP endorsing an easy exciton migration. The EPR results of the pure polymer supported that as well. However, as all these analytical studies were conducted in solid-state, defect-induced rapid exciton recombination was observed. The highly hierarchical porosity (as calculated from the NLDFT plot) further added to this radiative energy loss.

Nonetheless, a high surface area and rich porosity content favored the catalysis as well through augmenting catalyst-substrate contact. Of note, the extensive mesopores present in the material eased the effective mass transport during catalysis. However, one can observe the decisive role of reaction solvent and reactant concentration in catalysis. Apart from the obvious reachability aspect mentioned above, it also played a critical role in modulating the property and activity of AzoCPP in the catalytic medium. One of the standard procedures for better photocatalytic activity is chemical cross-transferring of free charge-carrier to another system to mitigate charge recombination [3–5]. Here NBS and HE had precisely done that job. Aliphatic amines are well-known for their facile oxidation to N-radical cations, which had been exploited in numerous photocatalyses including the ones reported here. On the other hand, high ε_r of the reaction solvent can enhance the overall ε_r of a highly porous system provided the solvent can freely flow through those pores, which in turn enhances the exciton diffusion range. Water has the highest ε_r among common solvents (80), but it cannot go through the AzoCPP pores efficiently due to the intrinsic hydrophobicity of the scaffold. Acetonitrile, on the other hand, is one of the few organic solvents with high ε_r values (37.5) and is miscible to water. Therefore, the acetonitrile-water mixed solvent would be a great option to increase the exciton diffusion range of the system, enhancing photocatalytic activity while maintaining the holistic green nature of the protocol [40]. The screening of both catalyses indeed shown that the solvents with high ε_r values manifested better catalytic performance.

However, it should be noted that ε_r is one of the many aspects to consider while screening solvents during catalysis. Typically, the relative solvolytic stabilization of reaction intermediates/transition states is another key feature of reaction solvents. Additionally, the proton transfer ability of the solvents played important role in these catalyses as well. The material was recycled 5 times for each catalysis and recorded only a nominal drop in the catalytic activity in either case suggesting the innate sustainability of the polymer (Figure S8).

3. Materials and Methods

3.1. General Methods

Solid-state ^{13}C-CP/MAS NMR spectrum analysis was measured on a Bruker Advance 400 DSX spectrometer (Ghent, Belgium). Cross Polarization Magic Angle Spinning (CP/MAS) was performed at MAS of 10 kHz in a 4 mm zirconia rotor. TPPM decoupling was used for acquisition. ATR FT-IR spectroscopy was carried out on a Bruker Vertex 80 V FT-IR spectrometer. The adsorption-desorption isotherms were analyzed by Micrometrics instrument (ASAP 2020) using ultrapure Ar (99.999%) at 77.3 K. Samples were degassed at 120 °C for 6 h at vacuum before analysis. Surface area values were calculated using Brunauer–Emmett–Teller (BET) method at $0.003 < P/P_0 < 0.05$ range (Ghent, Belgium). Pore size distributions were calculated from Ar sorption isotherms using the nonlocal density functional theory (NLDFT).

The morphology study was conducted by an S4800 field emission scanning electron microscope (FESEM, Hitachi, Ghent, Belgium), whereas the TEM analysis was carried out in a Philips CM20 microscope at 200 kV. Imaging and diffraction of the structure were

performed at a low electron dose for minimizing beam damage to the sample. The 3D topographic mapping of the selected area from the TEM image was performed on ImageJ after due scale calibration. Powder XRD analysis was performed on Bruker D8 Advance diffractometer with a copper Kα radiation source (λ = 1.54056 Å) at 40 kV and 45 Ma with 5 °/s scanning speed. The content of residual Pd in AzoCPP was determined by inductively coupled plasma optical emission spectra (ICP, Varian VISTAMPX, Ghent, Belgium).

UV-Vis absorption spectra were recorded in solid-state on Shimadzu UV-2600i UV-visible spectrophotometer. The fluorescence spectrum of AzoCPP was analyzed in solid-state on Hitachi F-7000 (Ghent, Belgium). Electron paramagnetic resonance (EPR) spectra were measured on Bruker PMX spectrometer at room temperature. For pure AzoCPP, the analysis was done in solid-state whereas, for catalytic intermediate assessment, a dispersion in acetonitrile was used. The cyclic voltammogram was investigated on a CHI-660E workstation using a typical three-electrode system. The results were referenced against the SCE electrode. Further, 0.1 M NBu_4PF_6 in acetonitrile was used as the electrolyte for the CV analysis. The CPP ink was prepared by dispersing 2 mg of the material in a 500 µL isopropanol/water (3:2 *v*/*v*) mixture using Nafion (50 µL) as the binder. A total of 15 µL of the ink was drop cast on a freshly polished glassy carbon electrode (surface area 0.0707 cm^2) and air-dried to prepare the working electrode. The theoretical HOMO and LUMO orbital distribution and potentials were calculated using the Materials Studio suite.

3.2. Synthesis of AzoCPP

A 250 mL round bottom flask equipped with a stir bar was loaded with (*E*)-1,4-diiodoazobenzene (1 eqv., 1 mmol), triethynyl benzene (0.7 eqv., 0.7 mmol), and *bis*-(triphenylphosphine)-palladium(II) chloride (3 mol%) in a 1:1 mixture of DMF and triethylamine (100 mL) under inert atmosphere. The mixture was sonicated at room temperature to obtain a homogeneous dispersion which was then heated to 90 °C for 72 h with constant stirring (800 rpm). After completion, the dark brown reaction mixture was cooled to room temperature and washed thoroughly with DMF, water, methanol, and acetone in a respective order to remove the unreacted monomers/oligomers or catalyst residues. The insoluble solid product was then sonicated in dil. acid and base solutions in MeOH for 1 h, washed again thoroughly with MeOH until the washing became neutral, and dried in vacuum for 12 h at 60 °C. ICP analysis of the AzoCPP network confirmed the presence of 63 ppm residual Pd.

3.3. General Procedure for Photocatalytic Oxidative Bromination

In a typical method, the aryl substrate (0.1 mmol), NBS (0.2 mmol), and AzoCPP (5 mg) were added to a 1.5 mL acetonitrile/water mixture (2:1) in a glass vial under air atmosphere and stirred to disperse the reactants. The reaction vessel was then exposed to a PL-XQ 350W (Ghent, Belgium) short-arc Xe lamp attached with a 400 nm band-pass filter. The distance between the lamp and the reaction mixture was maintained to be 10 cm. To nullify the photothermal effect, the reactions were carried out in a water bath maintained at room temperature. The reaction progress was monitored by TLC. After completion, the mixture was filtered off to collect the catalyst and the filtrate was washed with ethyl acetate, dried over Na_2SO_4, and subjected to gas chromatography (GC) for assessment (Ghent, Belgium).

3.4. General Procedure for Photocatalytic Dehydroxylation of Boronic Acid

In a typical method, the boronic acid substrate (0.1 mmol), Hantzsch ester (0.15 mmol), and AzoCPP (5 mg) were added to 2 mL acetonitrile/water mixture (4:1) in a glass vial under O_2 atmosphere (1 atm) and stirred to disperse the reactants. The reaction vessel was then exposed to a PL-XQ 350W short-arc Xe lamp attached with a 400 nm band-pass filter for 1d. The distance between the lamp and the reaction mixture was maintained to be 10 cm. To nullify the photothermal effect, the reactions were carried out in a water bath maintained at room temperature. The reaction progress was monitored by TLC. After completion, the reaction mixture was quenched with 0.5 M aqueous HCl and filtered off to collect the

catalyst. The filtrate was washed with ethyl acetate, dried over Na_2SO_4, and subjected to gas chromatography (GC) for assessment.

4. Conclusions

In summary, an azobenzene-based hierarchically porous high-surface-area photo-responsive conjugated porous polymer was synthesized as nano-sized particles with intrinsic structural defects. The synthesis, morphology, and structural aspects were thoroughly studied by state-of-the-art analytical techniques. The photo-triggered exciton separation and their defect-induced diffusion were corroborated by both experimental and theoretical justifications. These structure–property relations of the polymer were exploited by two photo-redox catalytic assays *viz.* oxidative bromination of arenes, and oxidative dehydroxylation of boronic acids. The catalytic observations and mechanisms were reasoned with relevant analytical studies and control experiments, and explained from the perspective of the structure and physicochemical properties of the polymer. Both catalytic protocols manifested wide substrate scopes.

Supplementary Materials: The supplementary figures (Figures S1 to S8), and tabulated data (Tables S1 to S4) are available online at https://www.mdpi.com/article/10.3390/catal11091064/s1. Figure S1: PXRD of AzoCPP. Figure S2: O1s XPS of AzoCPP. Figure S3: CV of AzoCPP. Figure S4: HOMO of AzoCPP molecular analog. Figure S5: LUMO of AzoCPP molecular analog. Figure S6: EPR of AzoCPP in dark and light. Figure S7: EPR of DMPO-superoxide adduct. Figure S8: Catalyst recycling. Figure S9: ^{1}H NMR spectra of Azo monomer. Table S1: Screening conditions for bromination. Table S2: Control experiments for bromination. Table S3: Screening conditions for dehydroxylation of boronic acids. Table S4: Control experiments for dehydroxylation of boronic acids.

Author Contributions: I.N., J.C. and P.V.D.V. conceptualized the project. J.C., I.N. and S.A. conducted the experiments and wrote the manuscript with inputs from P.V.D.V. All authors have read and agreed to the final version of the manuscript.

Funding: P.V.D.V., J.C. and I.N. acknowledge the FWO-Vlaanderen (Research Foundation Flanders) for financial support via the senior research project G020521N on photocatalysis. S.A. acknowledges financial support from the Ghent University BOF Doctoral Grant 01D04318.

Data Availability Statement: The data that support the findings of this study are available from the corresponding authors, [P.V.D.V., J.C. and I.N.], upon reasonable request.

Conflicts of Interest: The authors declare no conflict of interest.

References

1. Cooper, A.I. Conjugated microporous polymers. *Adv. Mater.* **2009**, *21*, 1291–1295. [CrossRef]
2. Xu, Y.; Jin, S.; Xu, H.; Nagai, A.; Jiang, D. Conjugated microporous polymers: Design, synthesis and application. *Chem. Soc. Rev.* **2013**, *42*, 8012–8031. [CrossRef] [PubMed]
3. Vilela, F.; Zhang, K.A.I.; Antonietti, M. Conjugated porous polymers for energy applications. *Energy Environ. Sci.* **2012**, *5*, 7819–7832. [CrossRef]
4. Taylor, D.; Dalgarno, S.J.; Xu, Z.; Vilela, F. Conjugated porous polymers: Incredibly versatile materials with far-reaching applications. *Chem. Soc. Rev.* **2020**, *49*, 3981–4042. [CrossRef]
5. Chakraborty, J.; Nath, I.; Song, S.; Mohamed, S.; Khan, A.; Heynderickx, P.M.; Verpoort, F. Porous organic polymer composites as surging catalysts for visible-light-driven chemical transformations and pollutant degradation. *J. Photochem. Photobiol. C Photochem. Rev.* **2019**, *41*, 100319. [CrossRef]
6. Xu, X.; Zhang, Q. Recent progress in covalent organic frameworks as light-emitting materials. *Mater. Today Energy* **2021**, *20*, 100635. [CrossRef]
7. She, P.; Qin, Y.; Wang, X.; Zhang, Q. Recent progress in external-stimulus-responsive 2D covalent organic frameworks. *Adv. Mater.* **2021**, 2101175. [CrossRef]
8. Zhi, Y.; Wang, Z.; Zhang, H.-L.; Zhang, Q. Recent progress in metal-free covalent organic frameworks as heterogeneous catalysts. *Small* **2020**, *16*, e2001070. [CrossRef] [PubMed]
9. Yao, C.-J.; Wu, Z.; Xie, J.; Yu, F.; Guo, W.; Xu, Z.J.; Li, D.-S.; Zhang, S.; Zhang, Q. Two-dimensional (2D) covalent organic framework as efficient cathode for binder-free lithium-ion battery. *ChemSusChem* **2019**, *13*, 2457–2463. [CrossRef] [PubMed]
10. Banerjee, T.; Podjaski, F.; Kröger, J.; Biswal, B.P.; Lotsch, B.V. Polymer photocatalysts for solar-to-chemical energy conversion. *Nat. Rev. Mater.* **2021**, *6*, 168–190. [CrossRef]

11. Wisser, F.M.; Berruyer, P.; Cardenas, L.; Mohr, Y.; Quadrelli, E.A.; Lesage, A.; Farrusseng, D.; Canivet, J. Hammett parameter in microporous solids as macroligands for heterogenized photocatalysts. *ACS Catal.* **2018**, *8*, 1653–1661. [CrossRef]
12. Kim, S.; Ogata, T.; Kurihara, S. Azobenzene-containing polymers for photonic crystal materials. *Polym. J.* **2017**, *49*, 407–412. [CrossRef]
13. Zhu, C.; Lu, Y.; Sun, J.; Yu, Y. Dynamic interfacial regulation by photodeformable azobenzene-containing liquid crystal polymer micro/nanostructures. *Langmuir* **2020**, *36*, 6611–6625. [CrossRef]
14. Nath, I.; Chakraborty, J.; Khan, A.; Arshad, M.N.; Azum, N.; Rab, M.A.; Asiri, A.M.; Alamry, K.A.; Verpoort, F. Conjugated mesoporous polyazobenzene–Pd(II) composite: A potential catalyst for visible-light-induced Sonogashira coupling. *J. Catal.* **2019**, *377*, 183–189. [CrossRef]
15. Nath, I.; Chakraborty, J.; Zhang, G.; Chen, C.; Chaemchuen, S.; Park, J.; Zhuiykov, S.; Han, T.; Verpoort, F. Understanding the roles of variable Pd(II)/Pd(0) ratio supported on conjugated poly-azobenzene network: From characteristic alteration in properties to their cooperation towards visible-light-induced selective hydrogenation. *J. Catal.* **2020**, *385*, 120–128. [CrossRef]
16. Gon, M.; Wakabayashi, J.; Nakamura, M.; Tanaka, K.; Chujo, Y. Preparation of near-infrared emissive π-conjugated polymer films based on boron-fused azobenzene complexes with perpendicularly protruded aryl substituents. *Macromol. Rapid Commun.* **2020**, *42*, 2000566. [CrossRef]
17. Tobin, J.M.; McCabe, T.J.D.; Prentice, A.W.; Holzer, S.; Lloyd, G.O.; Paterson, M.J.; Arrighi, V.; Cormack, P.A.G.; Vilela, F. Polymer-supported photosensitizers for oxidative organic transformations in flow and under visible light irradiation. *ACS Catal.* **2017**, *7*, 4602–4612. [CrossRef]
18. Luo, J.; Zhang, X.; Zhang, J. Carbazolic porous organic framework as an efficient, metal-free visible-light photocatalyst for organic synthesis. *ACS Catal.* **2015**, *5*, 2250–2254. [CrossRef]
19. Su, C.; Tandiana, R.; Tian, B.; Sengupta, A.; Tang, W.; Su, J.; Loh, K.P. Visible-light photocatalysis of aerobic oxidation reactions using carbazolic conjugated microporous polymers. *ACS Catal.* **2016**, *6*, 3594–3599. [CrossRef]
20. Takanabe, K. Photocatalytic water splitting: Quantitative approaches toward photocatalyst by design. *ACS Catal.* **2017**, *7*, 8006–8022. [CrossRef]
21. Noda, Y.; Merschjann, C.; Tarábek, J.; Amsalem, P.; Koch, N.; Bojdys, M.J. Directional charge transport in layered two-dimensional triazine-based graphitic carbon nitride. *Angew. Chem. Int. Ed.* **2019**, *58*, 9394–9398. [CrossRef]
22. Bässler, H.; Köhler, A. *Unimolecular and Supramolecular Electronics I: Chemistry and Physics Meet at Metal-Molecule Interfaces*; Metzger, R.M., Ed.; Springer: Berlin/Heidelberg, Germany, 2011; Volume 312, pp. 1–65.
23. Wang, Y.; Vogel, A.; Sachs, M.; Sprick, R.S.; Wilbraham, L.; Moniz, S.J.A.; Godin, R.; Zwijnenburg, M.A.; Durrant, J.R.; Cooper, A.I.; et al. Current understanding and challenges of solar-driven hydrogen generation using polymeric photocatalysts. *Nat. Energy* **2019**, *4*, 746–760. [CrossRef]
24. Pelzer, K.M.; Darling, S.B. Charge generation in organic photovoltaics: A review of theory and computation. *Mol. Syst. Des. Eng.* **2016**, *1*, 10–24. [CrossRef]
25. Tamai, Y.; Ohkita, H.; Benten, H.; Ito, S. Exciton diffusion in conjugated polymers: From fundamental understanding to improvement in photovoltaic conversion efficiency. *J. Phys. Chem. Lett.* **2015**, *6*, 3417–3428. [CrossRef] [PubMed]
26. Gregg, B.A. Charged defects in soft semiconductors and their influence on organic photovoltaics. *Soft Matter* **2009**, *5*, 2985–2989. [CrossRef]
27. Godin, R.; Wang, Y.; Zwijnenburg, M.A.; Tang, J.; Durrant, J.R. Time-resolved spectroscopic investigation of charge trapping in carbon nitrides photocatalysts for hydrogen generation. *J. Am. Chem. Soc.* **2017**, *139*, 5216–5224. [CrossRef] [PubMed]
28. Steinmann, S.N.; Melissen, S.T.A.G.; Le Bahers, T.; Sautet, P. Challenges in calculating the bandgap of triazine-based carbon nitride structures. *J. Mater. Chem. A* **2017**, *5*, 5115–5122. [CrossRef]
29. Lau, V.W.-H.; Yu, V.W.-Z.; Ehrat, F.; Botari, T.; Moudrakovski, I.; Simon, T.; Duppel, V.; Medina, E.; Stolarczyk, J.; Feldmann, J.; et al. Urea-modified carbon nitrides: Enhancing photocatalytic hydrogen evolution by rational defect engineering. *Adv. Energy Mater.* **2017**, *7*, 1602251. [CrossRef]
30. Noriega, R.; Rivnay, J.; Vandewal, K.; Koch, F.P.V.; Stingelin, N.; Smith, P.; Toney, M.F.; Salleo, A. A general relationship between disorder, aggregation and charge transport in conjugated polymers. *Nat. Mater.* **2013**, *12*, 1038–1044. [CrossRef]
31. Zhi, Y.; Li, K.; Xia, H.; Xue, M.; Mu, Y.; Liu, X. Robust porous organic polymers as efficient heterogeneous organo-photocatalysts for aerobic oxidation reactions. *J. Mater. Chem. A* **2017**, *5*, 8697–8704. [CrossRef]
32. Chakraborty, J.; Nath, I.; Verpoort, F. Pd-nanoparticle decorated azobenzene based colloidal porous organic polymer for visible and natural sunlight induced Mott-Schottky junction mediated instantaneous Suzuki coupling. *Chem. Eng. J.* **2019**, *358*, 580–588. [CrossRef]
33. Zhou, J.; Nomenyo, K.; Cesar, C.C.; Lusson, A.; Schwartzberg, A.; Yen, C.-C.; Woon, W.-Y.; Lerondel, G. Giant defect emission enhancement from ZnO nanowires through desulfurization process. *Sci. Rep.* **2020**, *10*, 4237. [CrossRef]
34. Wang, H.; Jiang, S.; Chen, S.; Zhang, X.; Shao, W.; Sun, X.; Zhao, Z.; Zhang, Q.; Luo, Y.; Xie, Y. Insights into the excitonic processes in polymeric photocatalysts. *Chem. Sci.* **2017**, *8*, 4087–4092. [CrossRef]
35. Ghosh, R.; Paesani, F. Unraveling the effect of defects, domain size, and chemical doping on photophysics and charge transport in covalent organic frameworks. *Chem. Sci.* **2021**, *12*, 8373–8384. [CrossRef] [PubMed]
36. Roessler, M.M.; Salvadori, E. Principles and applications of EPR spectroscopy in the chemical sciences. *Chem. Soc. Rev.* **2018**, *47*, 2534–2553. [CrossRef] [PubMed]

37. Saikia, I.; Borah, A.J.; Phukan, P. Use of bromine and bromo-organic compounds in organic synthesis. *Chem. Rev.* **2016**, *116*, 6837–7042. [CrossRef]
38. Dastan, A.; Tahir, M.N.; Ülkü, D.; Balci, M. Bromination of naphthalene and derivatives: High temperature bromination XI. *Tetrahedron* **1999**, *55*, 12853–12864. [CrossRef]
39. Rogers, D.; Brown, R.G.; Brandeburg, Z.C.; Ko, E.Y.; Hopkins, M.D.; Leblanc, G.; Lamar, A.A. Organic dye-catalyzed, visible-light photoredox bromination of arenes and heteroarenes using n-bromosuccinimide. *ACS Omega* **2018**, *3*, 12868–12877. [CrossRef] [PubMed]
40. Clarke, C.; Tu, W.-C.; Levers, O.; Bröhl, A.; Hallett, J.P. Green and sustainable solvents in chemical processes. *Chem. Rev.* **2018**, *118*, 747–800. [CrossRef] [PubMed]